journal of the mechanical behavior of biomedical materials 111 (2020) 104011

Contents lists available at ScienceDirect

Journal of the Mechanical Behavior of Biomedical Materials

journal homepage: http://www.elsevier.com/locate/jmbbm

Mechanical and morphometric study of mitral valve chordae tendineae and related papillary muscle

Shengda Chen [a,b,c], Candra Ratna Sari [a], Hao Gao [d], Yang Lei [e], Patrick Segers [b], Matthieu De Beule [b,f], Guixue Wang [a], Xingshuang Ma [a,*]

[a] College of Bioengineering, Chongqing University, Key Laboratory of Biorheological Science and Technology (Chongqing University), Ministry of Education, Chongqing, 400030, China
[b] IBiTech – BioMMeda, Department of Electronics and Information Systems, Ghent University, Ghent, Belgium
[c] Numerical Simulation Center, Microport, Shanghai, China
[d] School of Mathematics & Statistics, University of Glasgow, Glasgow, UK
[e] National Engineering Research Center for Biomaterials, Sichuan University, Chengdu, China
[f] FEops NV, Ghent, Belgium

ARTICLE INFO

Keywords:
Mitral valve
Papillary muscles
Chordae tendineae
Mechanical properties
Tensile test
Histology
Constitutive modeling

ABSTRACT

The mitral valve (MV) apparatus is a complex mechanical structure including annulus, valve leaflets, papillary muscles (PMs) and connected chordae tendineae. Chordae anchor to the papillary muscles to help the valve open and close properly during one cardiac cycle. It is of paramount importance to understand the functional, mechanical, and microstructural properties of mitral valve chordae and connecting PMs. In particular, little is known about the biomechanical properties of the anterior and posterior papillary muscle and corresponding chords. In this work, we performed uniaxial and biaxial tensile tests on the anterolateral (APM) and posteromedial papillary muscle (PPM), and their respective corresponding chordae tendineae, chordae^{APM} and chordae^{PPM}, in porcine hearts. Histology was carried out to link the microstructure and macro-mechanical behavior of the chordae and PMs. Our results demonstrate that chordae^{PPM} are less in number, but significantly longer and stiffer than chordae^{APM}. These different biomechanical properties may be partially explained by the higher collagen core ratio and larger collagen fibril density of chordae^{PPM}. No significant mechanical or microstructural differences were observed along the circumferential and longitudinal directions of APM and PPM samples. Data measured on chordae and PMs were further fitted with the Ogden and reduced Holzapfel - Ogden strain energy functions, respectively. This study presents the first comparative anatomical, mechanical, and structural dataset of porcine mitral valve chordae and related PMs. Results indicate that a PM based classification of chordae will need to be considered in the analysis of the MV function or planning a surgical treatment, which will also help developing more precise computational models of MV.

1. Introduction

The mitral valve (MV) is a complex structure including annulus, leaflets, papillary muscles (PMs), and chordae tendineae. The harmonious collaboration of the chordae and PMs plays an important role in the normal functioning of the mitral valve: the chordae connect the leaflets and PMs, assisting in maintaining a stable systolic coaptation of the mitral valve during the cardiac cycles, while PMs tether the valve leaflets to the ventricle wall to prevent prolapse. Chordal and PM rupture almost always results in flail leaflets and acute severe mitral regurgitation (Gabbay and Yosefy, 2010), which is a serious medical complication. A systematic clinical review by Gabbay and Yosefy analyzed and investigated the underlying major cause of chord rupture, identifying mitral valve prolapse and myxomatous degeneration as major causes (Gabbay and Yosefy, 2010). More and more, rather than replacing the valve by a prosthesis, the therapy of choice is to surgically correct ruptured chords by repairing or replacement (Bortolotti et al., 2012; Gammie et al., 2018). Therefore, it is of clinical interest to better understand the functional, mechanical and microstructural properties of mitral valve chordae and PMs.

Chordae are usually distinguished by their leaflet insertion locations as the primary (marginal) and secondary (basal and strut) chordae

* Corresponding author.
E-mail address: maxs@cqu.edu.cn (X. Ma).

https://doi.org/10.1016/j.jmbbm.2020.104011
Received 11 December 2019; Received in revised form 7 July 2020; Accepted 21 July 2020
Available online 30 July 2020

(Lomholt et al., 2002; Nielsen et al., 2011). The primary chordae attach to the free edges of the leaflet, which are thinner and shorter, and the secondary chordae insert into the central zones of the anterior and posterior leaflets, which are thicker and longer. All chordae are connected to the left ventricular wall by papillary muscles, which are labelled according to their projected position with respect to the mitral commissures as the anterolateral papillary muscle (APM) and the posteromedial papillary muscle (PPM). In most cases, the APM has a single head and dual blood supply from the left circumflex and left anterior descending coronary arteries. The PPM has commonly two heads and is either supplied by the right or circumflex coronary artery based on dominance (Morris et al., 2015; Stefanovski et al., 2012; Yamazaki et al., 2015).

There are many studies have focused on the asymmetry in anatomy and differences in mechanical properties based on the insertion location of the leaflet (Lam et al., 1970; Lomholt et al., 2002; Pokutta-Paskaleva et al., 2019; Ross et al., 2020; Zuo et al., 2016), leaflet type (Zuo et al., 2016) and chordal size (Liao and Vesely, 2003). For example, Liao and Vesely (2003) studied the size-related mechanical properties of porcine mitral valve chordae tendineae, and concluded that the dependency of the elastic modulus on chordae size can be explained by differences in fibril packaging. Early chordal uniaxial tests used the displacement of cross-head of grips as a measurement of elongation of samples (Kunzelman and Cochran, 1990; Liao and Vesely, 2003; Millard et al., 2011). The study by Ritchie et al. (2005) brought in the necessity of a non-destructive optical digital image correlation (DIC) based marker tracking system, which could reduce edge effects in stretch measurements. Using this technique, they tested strut chordae under physiological loading, and reported 46.2% difference in the strain calculation at mid-load (1 N) between the DIC measured and cross-head reported displacements. Using the DIC technique, five chords from 2 human cadavers have been tested by Prot et al. (2010). Both healthy and pathology samples were tested and used for finite element modelling of valve motion. Zuo et al. (2016), Pokutta-Paskaleva et al. (2019) and Ross et al. (2020) tested different kinds of chordae with DIC tracking systems. These recent studies (Pokutta-Paskaleva et al., 2019; Zuo et al., 2016) showed that chords of differing types vary largely in size, but do not have significantly different elastic and failure properties.

Many studies focused on the mechanical properties based on different chordae type or leaflet type while neglecting the relationship between chordae and PMs. Clinical studies (Cherian et al., 2014; Yamazaki et al., 2015) have found that the posterior PM (PPM) has a higher risk of necrosis and rupture in myocardial ischemia and infarction, which may relate to the differences in blood supply, but the underlying mechanism is still unknown. Only a few biomechanical studies have observed chordae property differences relating to PMs. For example, Ritchie et al. (2005) reported that strut chords which are connected to PPM are longer than those connected to the anterior PM (APM). Ross et al. (2020) performed a uniaxial tensile test on leaflet-chordae-papillary muscle entity, and the stretch of chords on left group was significantly higher than that of chords on the other side. Nielsen et al. (2005) measured porcine chordal forces by using dedicated miniature force transducers, and concluded that the strut chords connected to PPM experience a higher maximum tension than the strut chords connected to APM. Adams and O'Rourke (2015) and Askov et al. (2013); (2011) used force transducers to measure forces on papillary muscles in-vitro and in-vivo. Both of their results have shown that the two papillary muscles operate in different mechanical loading environments. Computational simulation based on precise experimental data has also been employed to study mechanical environments in chordae and PMs. For example, Wang and Sun (2012) reported that the tension of the APM is lower than the PPM at mid systole using a patient-specific mitral valve finite element model. The different mechanical environments and mechanical properties of both chordae and PPMs may play a role in MV dysfunction. To the best of our knowledge, there has not been a synergistic investigation of the mechanical properties of PMs and a papillary muscle-based classification of chordae.

Heart valve apparatus, including leaflets and PMs, also show regional biomechanical variation. Laurence et al. (2019) performed series of experiments on heart leaflets and reported that the central regions of the leaflet had a more anisotropic nature than edge regions in the MV, the material anisotropy of both anterior and posterior leaflets are of similar nature (Jett et al., 2018). Pokutta-Paskaleva et al. (2019) reported valve type related leaflet biomechanical differences with porcine samples. Pham found both the degree of anisotropy and stiffness of human left heart valves are higher than those of the right heart (Pham et al., 2017). Fatemifar et al. (2018) studied biomechanical properties of myocardial cell based apparatus including trabeculae carneae, PM, and myocardium of the human heart. They found that trabeculae carneae are significantly stiffer than myocardium, and left ventricle papillary muscles are stiffer than the left ventricle myocardium while there are little differences between right ventricle papillary muscles and myocardium.

In this study, we assessed the mechanical behavior of chordae and PM samples of the porcine heart, known to be an appropriate model for investigation of the human valve (Kunzelman et al., 1994). Mitral valve chordae were categorized and measured based on their insertion locations related to the PMs. Uniaxial tensile tests were utilized to analyze the mechanical properties of the chordae, and papillary muscle was studied using biaxial tensile tests. Masson's trichrome staining and transmission electron microscope (TEM) observations were carried out for histological and microstructure analysis. We aim to provide insight into the relation between papillary muscles and chordae relation in terms of anatomical and mechanical characteristics, and further improve our understanding of mitral valve function.

2. Methods

2.1. Tissue procurement

Forty fresh porcine hearts (weight 369.07 ± 68.24 g, 12 months old) were submerged in 4 °C phosphate-buffered saline (PBS) after being harvested from a local slaughterhouse in Chongqing (China) and delivered for testing. Specimens of mitral valve with papillary muscle were carefully dissected and cut open from the posteromedial commissure (Fig. 1A&B). The number of chords which are connected to the free edge of the leaflet and to the PM were counted. Based on their fan shape distribution, their coverage area on the leaflet free edge was measured. Both MV chords and left ventricle PM samples were isolated and kept at 37 °C PBS bath to mimic the valve physiological conditions before and during the test. All samples were tested within 24 h after harvesting.

2.2. Specimen classification and sectioning

2.2.1. Chordae tendineae

For each mitral valve apparatus, we have collected as many as possible chordae samples and categorized them, based on their insertion locations related to the PM (Fig. 1B) as chordae^{APM} and chordae^{PPM}, respectively. The length of individual chordae L_0 is defined by the load free distance from the origin in the papillary muscle to the insertion point on the leaflet, and was measured from digital images (Fig. 2A). The average diameter d of chordae was measured at three random locations with an optical microscope (Zeiss CL 6000LED) (Fig. 2B). The cross-sectional area A was calculated with $A = \pi r^2 = \frac{\pi d^2}{4}$ by assuming a circular shape of the chord. Fiducial markers were marked with a 1 cm gauge length (distance between two markers) around the central location of the sample using permanent marker for optical strain measurements (Fig. 2C).

2.2.2. Papillary muscle

APM and PPM samples were dissected from each heart. Approximately 2 mm thick PM slice specimens were cut with an 8 mm × 8 mm

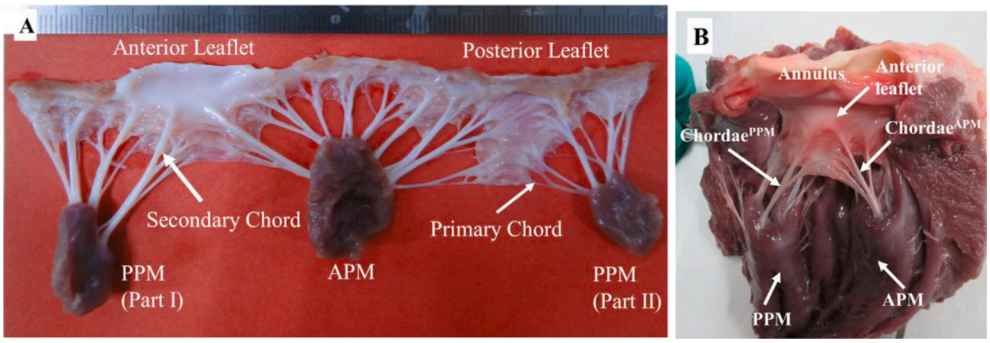

Fig. 1. A. representative sample of mitral valve, papillary muscles and connecting chordae; B. anatomical display of mitral valve in left ventricle, and relative position of APM, PPM and anterior leaflet.

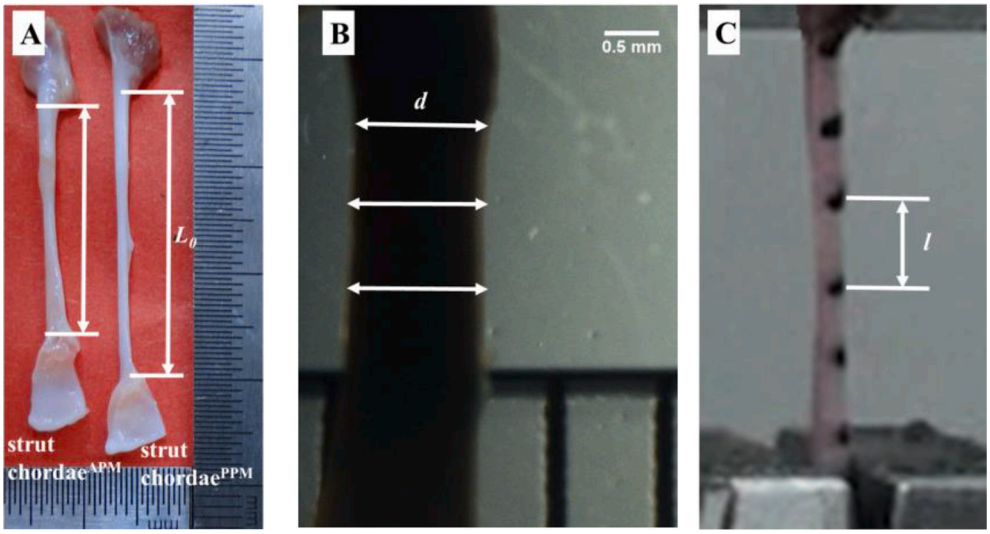

Fig. 2. A. the chord length measurement from scaled digital image; B. the chord diameter measurement from microscope; C. a captured image of uniaxial tensile test footage, black markers were added for strain measurement. *l* is the distance between two adjacent markers for strain calculation.

custom-made square cutter, with cross-fiber orientation in circumferential (x-axis) and fiber orientation in longitudinal direction (y-axis) (Fig. 3A). The thickness of the PM sample was measured with a digital caliper (±0.01 mm) three times before testing. Four glass bead markers were arranged in an array and adhered in the central region for optical strain tracking (Fig. 3B).

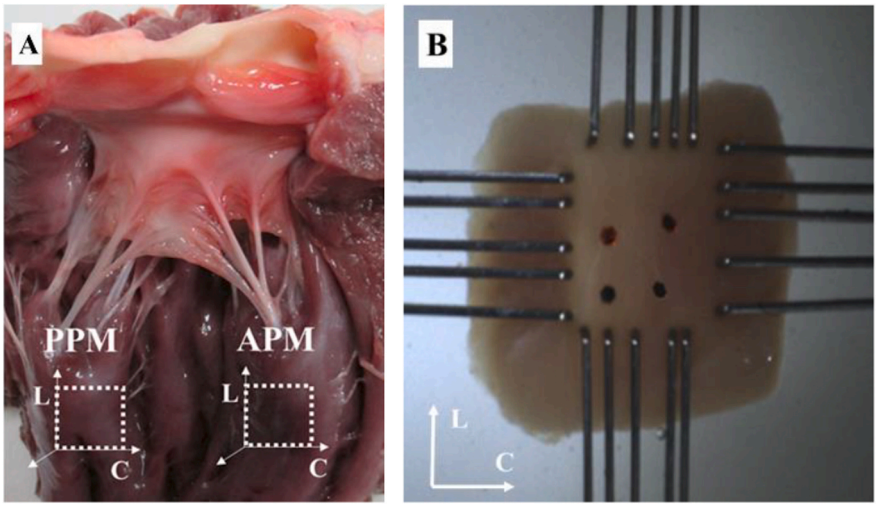

Fig. 3. A. the dashed square shows the location and orientation of PM samples for biaxial test, L and C illustrate the longitudinal and circumferential directions, respectively; B. a captured image of PM biaxial test image, the same color beads illustrate the circumferential direction.

2.3. Biomechanical testing

2.3.1. Uniaxial tensile test of chordae tendineae

Uniaxial tensile tests were carried out on 110 chord specimens from 11 hearts by Instron E1000 testing machine (Instron Industrial Products, US). Chordae with only a small part of papillary muscle and valve were sandwiched with sandpaper on both ends, and then were fixed onto a pair of pneumatic grips (2742–103, Instron Industrial Products, US) to make sure there was no slip between them. The chordae were pre-conditioned at 10 mm/min from 0 N to 2 N until the load-displacement curve was visibly repeatable (10 cycles). A 1080P high-definition (HD) digital video camera was fixed horizontally to record the locations of the markers (Fig. 2C) throughout the test with a constant rate of 25 frames/second, and triggered at the end of preconditioning. The specimens were stretched until failure or slippage from the grips with a loading rate of 10 mm/min and force sensor sampling rate of 10Hz. The target region and corresponding fiducial markers were manually selected where the rupture was occurred. Since some samples were short and ruptured outside of the optical markers or slipped from the grips, thus only 44 samples were counted for tangent modulus (TM) calculation.

2.3.2. Biaxial tensile test of papillary muscle

Planar biaxial tensile tests were conducted with a CellScale BioTester (Waterloo, ON, Canada) with 10 N load-cell. Rakes with five parallel hooks fixed each side with an effective testing region of 4 mm × 4 mm. The circumferential and longitudinal direction were aligned with the x and y direction, respectively (Fig. 3A and B).

Firstly, PM specimens were stretched up to 15% strain and released fully for 8 complete cycles for preconditioning. Then the specimens were stretched to 40% strain with a maximum speed of 4.8 mm/min in order to cover the physiological condition (Fatemifar et al., 2018; Urheim et al., 2000). 1:1 stretch ratio on two directions was applied to analyze the anisotropic behavior of the tissue. The displacement of markers and corresponding tensile forces were recorded for all loading schemes and used for stress and strain analysis (Fig. 3B). Assuming incompressibility and neglecting the shear stress, the biaxial test measured the force and correlate displacement data for quantifying the Cauchy stress and stretch.

2.4. Stress and strain analysis

By assuming chordae is incompressible, for uniaxial experiments, we have

$$\mathbf{F} = \begin{bmatrix} \lambda_1 & 0 & 0 \\ 0 & \frac{1}{\sqrt{\lambda_1}} & 0 \\ 0 & 0 & \frac{1}{\sqrt{\lambda_1}} \end{bmatrix} \text{ and } \sigma_{11} = \lambda_1 \frac{f}{A_0} \tag{1}$$

where $\mathbf{F}$ is the deformation gradient tensor and $\lambda_1 = \frac{l}{l_0}$ is the stretch ratio along the stretching direction, l_0 and l are the initial and current distances between two markers after preconditioning, and f is the applied force along stretching direction. For chordae, A_0 is the cross-sectional area in the reference state, and equals to $\pi {R_0}^2$, where R_0 is the radius of the chordae.

For biaxial experiments, we have

$$\mathbf{F} = \begin{bmatrix} \lambda_1 & 0 & 0 \\ 0 & \lambda_2 & 0 \\ 0 & 0 & \lambda_3 \end{bmatrix} = \begin{bmatrix} \lambda_1 & 0 & 0 \\ 0 & \lambda_2 & 0 \\ 0 & 0 & \frac{1}{\lambda_1 \lambda_2} \end{bmatrix} \tag{2}$$

and

$$\sigma_{11} = \frac{f_1}{A_1} = \lambda_1 \frac{f_1}{A_0}$$
$$\sigma_{22} = \lambda_2 \frac{f_2}{A_0} \tag{3}$$

where λ_1, λ_2, and λ_3 are the principal stretches on each direction. For incompressible material $\lambda_1\lambda_2\lambda_3 = 1$, therefore $\lambda_3 = {}^1/_{\lambda_1\lambda_2}$. A_1 is the current cross-sectional area, and A_0 is the initial cross-sectional area for biaxial test samples with $A_0 = T_0.l_0$, in which T_0 is the thickness, l_0 is the length of the sample's effective test region. f_1 and f_2 are the loads measured by the load cell in circumferential and longitudinal direction.

After obtaining the Cauchy stress - stretch curve for each specimen, we calculated the TM for each sample by the slope of the post-transition linear range of the Cauchy stress - stretch curve as shown in Fig. 4 (Pokutta-Paskaleva et al., 2019; Zuo et al., 2016). The built-in least-square fitting function in MATLAB was used for determining TM. Ultimate tensile stress (UTS) and maximum stretch λ_{max}, which represent the maximum Cauchy stress and maximum stretch that can be reached by a chordae sample were measured and then compared in our study.

2.5. Image tracking for stretch calculation

For uniaxial tensile tests, the distances between two fiducial markers were tracked and computed using an in-house developed MATLAB code (R2015b MathWorks Inc., US) for stretch calculation. Detailed steps of extracting the stretch ratio from recorded images are described below:

- Step 1: import image files from one sample experiment (1, 2, …, N);
- Step 2: manually determine the target region with a cropped window using the MATLAB *imcrop()* function, see Fig. 5A;
- Step 3: load cropped image in sequence from the beginning or any other time with the window size determined in step 2, and convert it into greyscale shown in Fig. 5B. It can be found that the marker regions appear dark, and the unmarked chordae and the background are brighter than the markers;
- Step 4: the image is further binarized into black and white by applying *kmeans()* function with 2 clusters (the cluster with lower pixel intensity to be black, and the other to be white). Two marker regions (black) can be readily identified as shown in Fig. 5C;

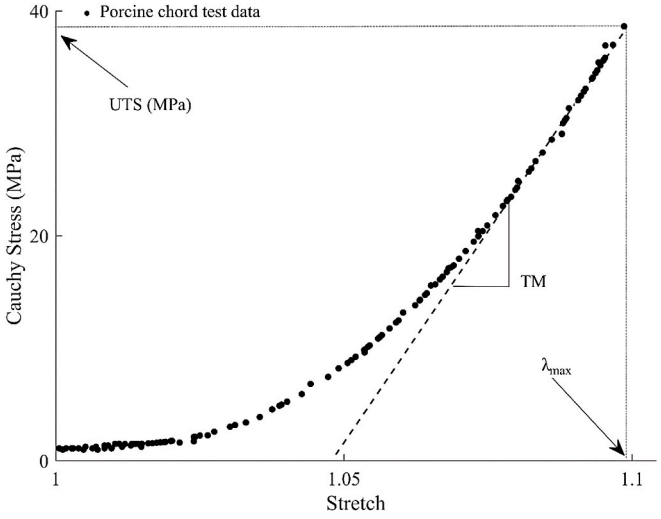

Fig. 4. Experimental Cauchy stress - stretch data of a chordal sample with illustration of the TM calculation by linear fitting to the post-transition linear range of the curve, ultimate tensile stress (UTS) and maximum stretch λ_{max} represent the maximum Cauchy stress and maximum stretch can be reached by a chordae sample.

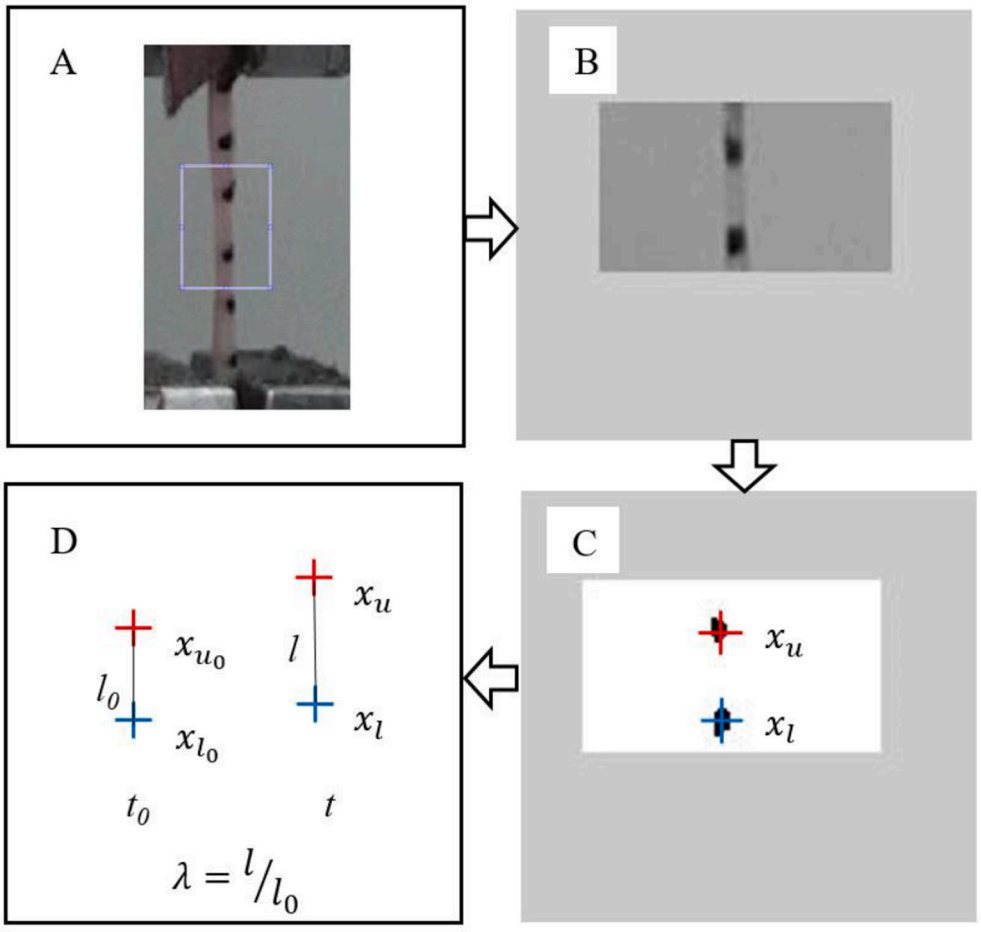

Fig. 5. Pipeline of extracting the stretch ratio during a uniaxial test from recorded sequence images. A: An original image at the end with the cropped rectangle; B: A cropped image with two markers appearing in dark; C: Tracked two markers after thresholding process, x_l is the centroid of the bottom marker and x_u is the centroid of the upper marker; D: Calculation of λ from tracked marker positions.

- Step 5: locate the two markers in Fig. 5C by finding the largest two dark regions using a conventional 8-neighbor region growing method implemented in MATLAB. The two black regions will be further reviewed later if manual correction is needed;
- Step 6: calculate the centroids of the two black regions, with the bottom one for x_l and the upper one for x_u, as indicated in Fig. 5C;
- Step 7: repeat Steps 3–6 until for the last image;
- Step 8: calculate the stretch ratio $\lambda = l/l_0$, in which l_0 is the initial distance between the two markers obtained from the first image, and l is the distance between the two markers during stretching. Fig. 5D schematically illustrates how λ is calculated. It is then followed by cubic spline space curve fit function *cscvn()* in MATLAB for strain calculation;

For biaxial tensile tests, we apply the built-in DIC module in the software LabJoy of BioTester to track and calculate the marker's displacements for strain calculation.

2.6. Constitutive models

The stress - stretch relationship of chordae was fitted to the one term Ogden strain energy function (Ogden, 1997), that is

$$W = \frac{\mu}{a}\left(\lambda_1^a + \lambda_2^a + \lambda_3^a - 3\right) \tag{4}$$

where μ and a are material constants, N is a positive integer. In a uniaxial tensile test, the Cauchy stress along the stretching direction is

$$\begin{cases} \sigma_{11} = \mu\lambda^a - p \\ \sigma_{22} = \sigma_{33} = \mu\lambda^{-\frac{1}{2}a} - p \end{cases} \tag{5}$$

in which p is a Lagrange multiplier to enforce the incompressibility of the chordae (Holzapfel, 2000), which can be obtained by assuming $\sigma_{22} = \sigma_{33} = 0$, that is $p = \mu\lambda^{-\frac{1}{2}a}$,thus,

$$\sigma_{11} = \mu\left(\lambda^a - \lambda^{-\frac{1}{2}a}\right) \tag{6}$$

A strain invariant-based constitutive law derived from the widely-used myocardial model developed by Holzapfel and Ogden (2009) is used for characterizing anisotropic hyper-elastic behaviors of PM samples, denoted the reduced Holzapfel-Ogden (reduced HO) model,

$$W = \frac{a}{2b}e^{b(I_1-3)} + \frac{a_f}{2b_f}\left(e^{b_f\left(I_f-1\right)^2} - 1\right) + p(J-1) \tag{7}$$

where a, b, a_f, and b_f are material constants, p is the Lagrange multiplier to enforce the incompressibility, that is by enforcing $J = \det(\mathbf{F}) = 1$. This way has been widely used in the literature when modelling incompressible soft tissue (Fan and Sacks, 2014). $I_1 = {\lambda_1}^2 + {\lambda_2}^2 + \left(\frac{1}{\lambda_1\lambda_2}\right)^2$, and $I_f = \mathbf{f}_0 \otimes \mathbf{f}_0 : \mathbf{C} = {\lambda_1}^2$ by assuming $\mathbf{f}_0 = [1,\ 0,\ 0]'$. $\mathbf{f}_0$ is the unit vector that defines the preferential direction of fibers in PM samples in the reference configuration, and $\mathbf{C}$ is the right Cauchy-Green tensor

$$\mathbf{C} = \begin{bmatrix} {\lambda_1}^2 & 0 & 0 \\ 0 & {\lambda_2}^2 & 0 \\ 0 & 0 & \left(\frac{1}{\lambda_1\lambda_2}\right)^2 \end{bmatrix} \tag{8}$$

Based on Eqs. (7) and (8), the Cauchy stress tensor can be expressed as $\boldsymbol{\sigma} = \frac{1}{\det(\mathbf{F})}\frac{\partial W}{\partial \mathbf{F}}\mathbf{F}^T$, from which we have the stress components along the fiber direction (σ_{11}), the cross fiber direction (σ_{22}) and the normal direction (σ_{33}) as the followings

$$\begin{cases} \sigma_{11} = ae^{b(I_1-3)}{\lambda_1}^2 + 2a_f\left(I_f^* - 1\right)e^{b_f\left(I_f^*-1\right)^2}{\lambda_1}^2 - p \\ \sigma_{22} = ae^{b(I_1-3)}{\lambda_2}^2 - p \\ \sigma_{33} = ae^{b(I_1-3)}\left(\frac{1}{\lambda_1\lambda_2}\right)^2 - p \end{cases} \tag{9}$$

in which $I_f^* = \max(I_f, 1)$, which means collagen fibers will not bear any load when compressed. By assuming $\sigma_{33} = 0$, we have $p = ae^{b(I_1-3)}\left(\frac{1}{\lambda_1\lambda_2}\right)^2$, and

$$\begin{cases} \sigma_{11} = ae^{b(I_1-3)}{\lambda_1}^2 + 2a_f\left(I_f^* - 1\right)e^{b_f\left(I_f^*-1\right)^2}{\lambda_1}^2 - ae^{b(I_1-3)}\left(\frac{1}{\lambda_1\lambda_2}\right)^2 \\ \sigma_{22} = ae^{b(I_1-3)}{\lambda_2}^2 - ae^{b(I_1-3)}\left(\frac{1}{\lambda_1\lambda_2}\right)^2 \end{cases} \tag{10}$$

Note that this is a reduced HO model, as we only included I_1 and I_f in this study by assuming that PM is transversely isotropic, while the original Holzapfel and Ogden model used extra strain invariants along other directions because of the highly layered fiber structure (Holzapfel and Ogden, 2009, 2010). Applications of their models can be found in recent studies (Gao et al., 2015; Guan et al., 2019; Sack et al., 2018).

The material constants for chordae and PM were determined by fitting the above two strain energy functions with corresponding experimental data. For each sample, we fitted all experimental data altogether and inversely determined one set of material parameters with a minimal deviation from all experiment data points using the least-square method,

$$\underset{\boldsymbol{\beta}}{\operatorname{argmin}} \sum_{m=1}^{M} [\sigma_m(\boldsymbol{\beta}) - \widehat{\sigma}_m]^2 \tag{11}$$

in which $\widehat{\sigma}_m$ is the measured stress, σ_m is the corresponding predicted stress from a strain energy function with the material parameter set $\boldsymbol{\beta}$, and M is the total number of data points from one sample. The data points were fitted based on the Levenberg-Marquardt nonlinear regression algorithm using the MATLAB function *lsqnonlin()*. To determine the variability of material parameters during the fitting procedure, a randomized initialization strategy was used with 50 sets of initial values drawn from the predefined parameter ranges. We chose $\mu \in [0\ 200]$ MPa, $a \in [0\ 200]$ for the Ogden model, and $a,\ a_f \in [0\ 200]$ kPa, $b,\ b_f \in [0\ 200]$ for the reduced HO model. For each specimen, the final optimized parameters are expressed using mean ± standard deviation from the 50 randomly generated initial values.

2.7. Histological analysis

2.7.1. Chordae tendineae

Following mechanical testing, 82 chord specimens were fixed within 4% glutaraldehyde in PO_4 buffer (pH 7.4) for 24 h, dehydrated with graduated concentrations of ethanol and embedded in paraffin. 5 μm thick cross-sectional sections were cut in the middle of the collagen core divided by the total chords and Masson's trichrome stain was carried out in order to distinguish among collagen, elastin, and cellular nuclei. All slides were observed with conventional bright field microscopy using the Zeiss CL 6000LED microscope imaging system (Nikon Corp, Japan) with magnifications of 40 × , 100 × , and 400 × . All images had a final image resolution of 1280 × 1024 pixels and a 48-bit intensity resolution. From Masson's trichrome stain, the collagen was stained blue. Cellular nuclei were stained dark brown, and muscle fibers and cytoplasm were stained red. Images were taken to measure the cross-sectional area of chordae sample and that of central core of collagen bundles. The collagen core area ratio was then calculated by the area of collagen core divided by total area of chordae.

We follow the methodology of Liao and Vesely (2003); (2007) for quantifying collagen fibril ultra-structure, which can illustrate the content of chordal load effect ingredient (Liao and Vesely, 2003) and stretch related ultra-structural change (Liao and Vesely, 2007). 21 chordal specimens from 3 hearts were processed for transmission electron microscopy (TEM) observation. They were trimmed and fixed with 2.5% glutaraldehyde, dehydrated with graduated concentration of ethanol and propylene oxide, and then embedded in Epon. 85 nm thick cross-sectional slides for each chord were then cut with a diamond knife, mounted on uncoated grids and then stained with uranyl acetate and lead citrate. Specimens were then observed with a Thermo Fisher TEM (Talos F200S, Thermo Fisher scientific, US) with magnifications of 25, 000 × 3 images were randomly taken from samples. Collagen fibril diameter, density and area occupation ratio were measured and calculated for each image. Collagen fibril density was defined as fibril amount per unit area. Collagen fibril area occupation ratio was defined as the total cross-sectional area of the fibrils divided by the total area of the image.

2.7.2. Papillary muscle

16 p.m. specimens were harvested from 4 hearts for Masson's trichrome staining in both longitudinal and circumferential directions. Using the same process as for the chordae, 5 μm thick square sections of PM sample were cut in the center of PM along the circumferential and longitudinal direction. Myocyte diameter, number and occupation ratio were measured from 8 randomly selected regions from each section in perpendicular to circumferential direction. Quantity of cell only include cell with nucleus. Myocyte occupation ratio was computed from the total cross-sectional area of myocytes and the total area of the image in both directions. The collagen content was measured from above mentioned samples and quantified as the percentage of collagen occupied area divided by the total area of the sample. All slides were observed with conventional bright field microscopy using the Zeiss CL 6000LED microscope imaging system (Nikon Corp, Japan). Image processing and measurement for chordae and PM were done with ImageJ (National Institutes of Health, USA).

2.8. Statistics

All measurements were reported as the mean and standard deviation, except Cauchy stress – stretch responses were presented as the mean and standard error of the mean. Chordal tangent modulus was calculated with linear regression analysis using least square fitting. Shapiro-Wilk tests were used to assess the normality of all data. Differences between two normally distributed groups were determined with the unpaired Student's *t*-test. The Wilcoxon signed-rank test and Mann-Whitney rank sum test were used for nonparametric data comparison. Correlation between chord size (length and diameter) and biomechanical parameter tangent modulus was tested with Pearson's correlation coefficient. Statistical analysis was performed using SigmaPlot (V14.0 Systat Software Inc., US). Statistically significant difference was accepted at $p < 0.05$ level.

3. Results

3.1. Anatomical measurements and morphological properties

The chord samples of this study were from 17 hearts. The anatomical measurements of chordae tendineae are illustrated in Table 1.

STD: standard deviation; λ_{max}: maximum stretch; UTS: ultimate tensile strength; p-value indicates difference between chordae^{APM} and chordae^{PPM}, statistically significant difference is annotated in bold, N indicates the number of samples.

Chordae form a tree root distribution from PM to leaflet, and the amount of chordae branches connected on the leaflet side is about 2 times more than that of chordae on the papillary muscle side ($p < 0.001$). There are more chords connected to APM than PPM, but neither the amount of chords connected to APM and PPM on the papillary muscle side ($p = 0.83$) nor on the leaflet side ($p = 0.25$) are statistically different. The chordae^{APM} coverage ratio on leaflet free edge is significantly larger than that of chordae^{PPM} ($p = 0.03$). Measurements of chordae diameter and length show that there is no significant difference in diameter ($p = 0.82$) between chordae^{APM} and chordae^{PPM}, but chordae^{PPM} are significantly longer than chordae^{APM} ($p < 0.001$). 39 p.m. samples were obtained from 20 hearts. The average thickness of samples is 1.67 ± 0.41 mm (1.68 ± 0.43 mm for APM and 1.66 ± 0.39 mm for PPM).

3.2. Biomechanical properties: chordae tendineae

3.2.1. Mechanical tests

The mean and standard deviation of Cauchy stress – stretch of APM and PPM chordae are shown in Fig. 6 in the range from 1 to 1.08, which is the common stretch range that could be achieved by all chordae. The tangent modulus of chordae tendineae is given in Fig. 7 and Table 1. Chordae^{PPM} is significantly stiffer than chordae^{APM} ($p = 0.037$), while both diameter ($p = 0.50$) and length ($p = 0.97$) have no correlation with tangent modulus. Chordal maximum stretch and ultimate tensile strength are given in Table 1, and no significant differences are observed between chordae^{PPM} and chordae^{APM} ($p > 0.05$).

In Table 2, the chordal TM and maximum stretch (λ_{max}) are compared with other published studies obtained with similar experimental protocols, such as using DIC for stretch measurements. For the human samples, the TM of hypertrophic obstructive cardiomyopathy (HOCM) pathological samples was much lower than that of healthy samples, and their maximum stretch was 5 times bigger (Prot et al., 2010). Interestingly, Zuo et al. (2016) reported that maximum stretch was much larger in aged human samples compared to the study of Prot

Table 1
Descriptive statistics and comparisons of morphological and mechanical properties between chordae^{APM} and chordae^{PPM}, including chordal number on PM side and leaflet side, percentage of chord coverage of leaflet free edge and annulus, sample average diameter and length, sample number for biomechanical test (N), mean and standard deviation of average tangent modulus, λ_{max}, and UTS.

		Mean ± STD		
	ALL	chordae^{APM}	chordae^{PPM}	p-value
Chordal number				
PM side	17.31 ± 3.28	11.23 ± 2.24	8.23 ± 2.05	0.83
Primary chordae		4.31 ± 1.49	2.23 ± 0.83	0.86
Secondary chordae		6.92 ± 1.50	6.00 ± 1.87	0.71
leaflet side	48.46 ± 5.55	26.38 ± 5.12	21.15 ± 5.8	0.25
Leaflet coverage ratio (%)	–	51.58 ± 3.35	48.42 ± 3.35	**0.03**
N	110	57	53	
Diameter (mm)	0.66 ± 0.21	0.66 ± 0.20	0.65 ± 0.21	0.82
Length (mm)	18.07 ± 3.55	16.04 ± 2.16	20.56 ± 3.35	**<0.001**
N	44	24	20	–
TM (MPa)	328.12 ± 195.14	272.31 ± 157.26	395.09 ± 218.13	**0.037**
λ_{max}	1.14 ± 0.12	1.12 ± 0.09	1.15 ± 0.13	0.23
UTS (MPa)	30.72 ± 11.3	31.04 ± 11.13	32.12 ± 10.46	0.72

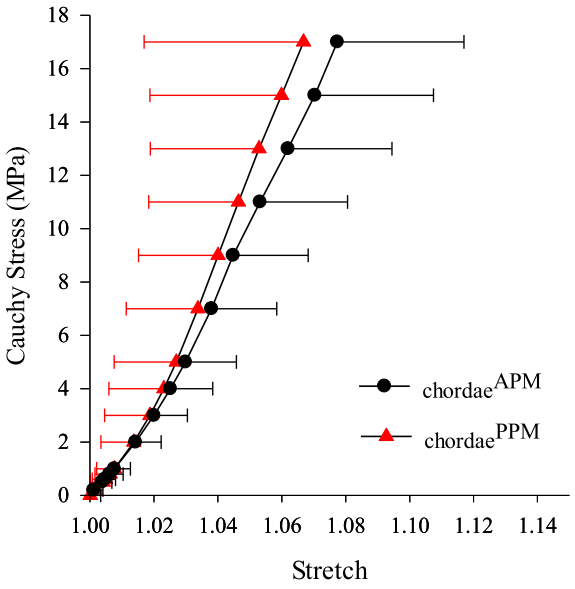

Fig. 6. The mean and standard error on the mean of the Cauchy stress – stretch responses of (A) chordae^{APM} and (B) chordae^{PPM}.

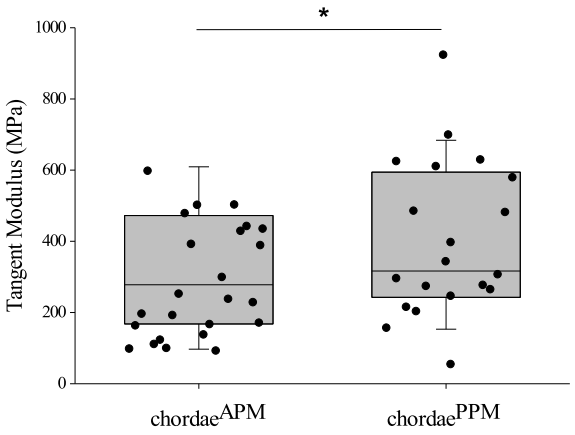

Fig. 7. The mean and standard deviation of the tangent modulus for chordae^{APM} and chordae^{PPM} *. Chordae^{PPM} are significantly stiffer than chordae^{APM}.

Table 2
Comparison of the post-transition mechanical properties with published studies.

	species	number	TM (MPa)	number	λ_{max}
Prot et al., 2010	human	3	254.39	3	0.04
	HOCM human	2	33.06	2	0.21
Zuo et al., 2016	aged human	151	358.81	35	0.21
	ovine	93	408.72	8	0.37
Pokutta-Paskaleva et al., 2019	porcine	–	154–198	–	–
Our study	porcine	44	328.12 ± 195.14	44	0.15 ± 0.15

HOCM: hypertrophic obstructive cardiomyopathy; -: means not provided.

et al. (2010). Previous study from ovine (Zuo et al., 2016) and our study from porcine showed that TM and the maximum stretch are comparable to the value reported in aged human study. In fact, our measurements are closer to human observations of both studies from Prot et al. (2010) and Zuo et al. (2016). Table 2 further suggests that there are species difference and subject variation in the mechanical properties of chordae.

3.2.2. Constitutive modelling

Fig. 8 shows an example of fitting the Ogden model to the mechanical behavior of chordae. The estimated parameters for all chordae can be found in the Appendix Table A1. The standard deviation is almost negligible for all samples, suggesting a good determinability is achieved. The corresponding average material parameters are summarized in Table 3, which are comparable to the reported values of recent studies (Pokutta-Paskaleva et al., 2019; Ross et al., 2020; Zuo et al., 2016). As the same as the TM values, our results are closer to human material parameters. Both μ and α are slightly higher in chordae^{PPM} than in chordae^{APM}.

3.2.3. Microstructure analysis

Chordae are composed of collagen fibers, which are densely packed in the innermost core and a thin spongiosa elastin layer outside. The collagen and elastin content can be qualitatively estimated from collagen area ratio and elastin area ratio, as shown in Table 4. The collagen ratio of chordae^{APM} is significantly smaller than that of chordae^{PPM} ($p = 0.02$) from Masson stain results (Fig. 9), which could partially explain larger TM in choardae^{PPM} than in chordae^{APM}.

STD: standard deviation; p-value indicates difference between chordae^{APM} and chordae^{PPM}, statistically significant difference is annotated in bold, N indicates amount of sample.

The average collagen fibril diameter of chordae^{APM} is significantly larger than that of chordae^{PPM} ($p < 0.001$) from TEM image (Fig. 10). Also, the average collagen fibril density of chordae^{APM} is significantly smaller than that of chordae^{PPM} ($p < 0.001$). When comparing area percentage occupied by chordal collagen fibrils, there is no significant difference between chordae^{APM} and chordae^{PPM} ($p = 0.76$). TEM results are illustrated in Fig. 11 and summarized in Table 4. From the microstructural analysis, we can find that chordae^{PPM} have higher collagen density and larger area ratio than chordae^{APM}, while the average collagen fibril diameter is smaller. We believe that these microstructure differences could explain differences in their passive biomechanical properties.

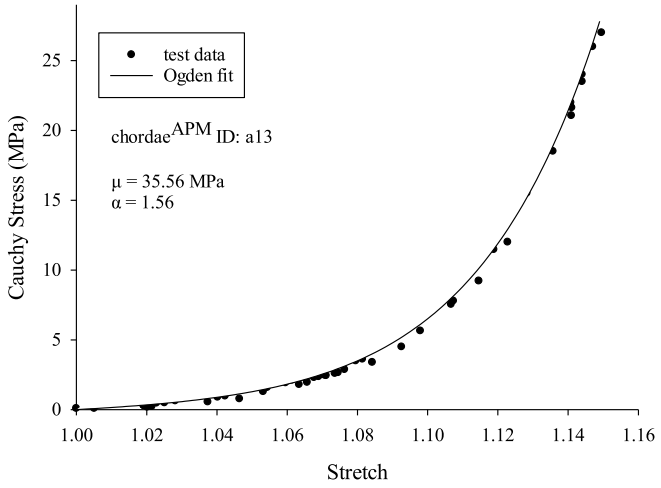

Fig. 8. Cauchy stress - stretch curve of chord^{APM} fitted with Ogden strain energy function under uniaxial stretch.

Table 3
The mean and SEM of the Ogden model material parameters for both chordae^{APM} and chordae^{PPM}, together with comparisons to other studies in the literature.

	ALL		chordae^{APM}		chordae^{PPM}	
	mean	SEM	mean	SEM	mean	SEM
μ(MPa)	9.74	1.58	8.63	2.28	11.06	2.15
A	46.98	6.83	43.24	6.92	51.48	12.68
other studies in the literature		species		μ (MPa)		α
Zuo et al. (2016)		Ovine		0.30–0.85		11.70–28.03
Zuo et al. (2016)		Human		8.39–9.61		22.04–30.86
Pokutta-Paskaleva et al. (2019)		Porcine		<49.34		0.41–68.21
Ross et al. (2020)		Porcine strut		<0.58		87.5–407.6

Table 4
Descriptive statistics and comparisons of histological properties between chordae^{APM} and chordae^{PPM}. Mean and standard deviation of average tangent modulus; sample number for Masson's trichrome stain (n), collagen area ratio; collagen fibril average diameter, average density, and area percentage occupation were illustrated.

	Mean (SD)			
	ALL	chordae^{APM}	chordae^{PPM}	p-value
N	82	43	39	–
collagen area ratio (%)	81.13 ± 7.91	79.66 ± 7.95	82.74 ± 7.64	**0.02**
N	60	28	32	–
Diameter (nm)	42.94 ± 5.55	45.82 ± 5.08	40.59 ± 4.82	**<0.001**
density (um^{-2})	169.56 ± 38.41	149.97 ± 32.76	185.60 ± 35.50	**<0.001**
area percentage occupation (%)	30.00 ± 4.74	30.38 ± 3.66	29.68 ± 5.51	0.76

3.3. Biomechanical properties: papillary muscle

3.3.1. Mechanical tests

The mean and standard deviation of the Cauchy stress - stretch of APM and PPM samples are illustrated in Fig. 12. The tangent modulus along the longitudinal direction under equal-biaxial stretch has a slightly higher value than that along circumferential orientation, but there is no significant difference (all $p = 0.32$, APM $p = 0.52$, and PPM $p = 0.46$). The PPM is stiffer than APM samples both in longitudinal ($p = 0.53$) and circumferential ($p = 0.62$) directions in general, but not significant (Fig. 13, Table 5).

3.3.2. Constitutive modeling

The reduced HO model can describe the mechanical behavior of papillary muscles. The estimated parameters for all PM samples can be found in the Appendix Table A2. Again, the standard deviation is almost negligible for most of samples, which indicates that a good determinability is achieved, in general. Fig. 14 shows one sample of PPM experiment data fitted with the reduced HO model. The corresponding average material parameters are summarized in Table 6.

3.3.3. Microstructure analysis

Myocyte diameter ($p = 0.13$), quantity of cells with nucleus ($p = 0.86$), the occupation ratio of myocytes ($p = 0.64$) are not different between APM and PPM (Fig. 15, Table 7). The collagen contents ($p = 0.45$) within APM and PPM are also similar.

4. Discussion

The papillary muscles and chordae tendineae work in harmony to

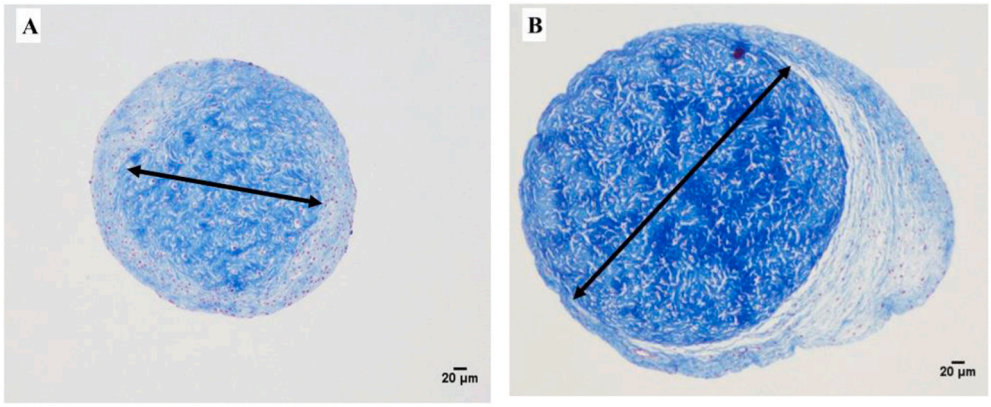

Fig. 9. Radial direction Masson's trichrome stain samples of chordae^{APM} (A) and chordae^{PPM} (B) from the same heart, the inside dark blue part marked with arrow is collagen core and the outside light blue part is elastin sheath.

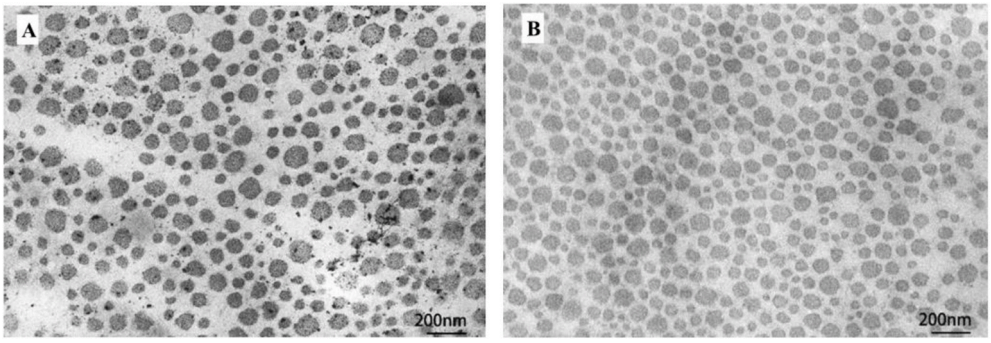

Fig. 10. TEM illustration of collagen fibril from (A) chordae^{APM} and (B) chordae^{PPM} samples of the same heart, dark dots are collagen fibril.

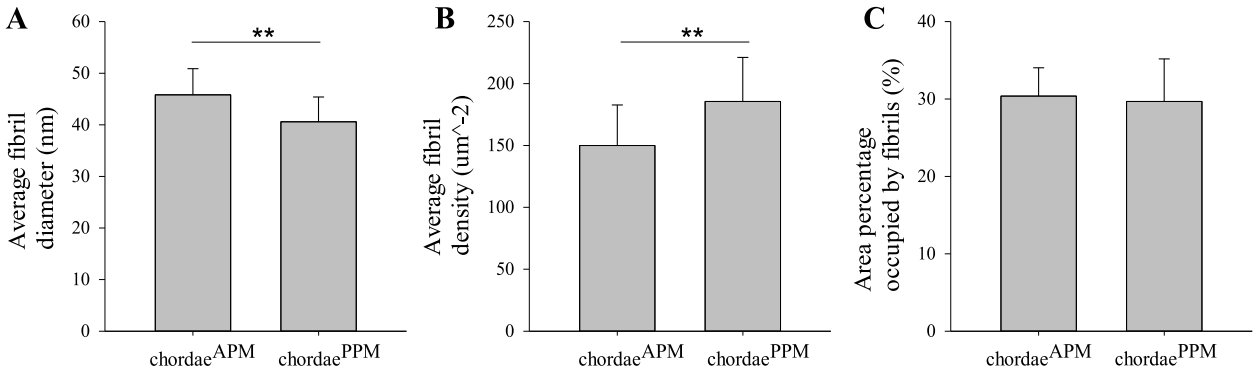

Fig. 11. Average fibril diameter (A), density (B) and area percentage occupied by fibrils (C) of both chordae^{APM} and chordae^{PPM}. **. Fibril of chordae^{PPM} are extremely significant thinner and higher density than fibril of chordae^{APM}.

maintain the normal functioning of the mitral valve, allowing unidirectional blood flow from the left atrium to the left ventricle in diastole, and preventing backflow in systole. It is of importance to know their characteristics and relationship between their anatomy and mechanical properties. The purpose of our study was to investigate the passive mechanical properties and micro-structural characteristics of PMs and chordae tendineae, along with comparisons of mechanical properties of chordae according to PM-based classification. We mainly focused on the passive properties of PMs and chordae. There are different approaches of measuring passive mechanical properties of soft tissue, including uniaxial (Ross et al., 2020; Tong et al., 2011) or biaxial testing (Laurence et al., 2019; Pokutta-Paskaleva et al., 2019) or shearing and torsion (Chen et al., 2018). Uniaxial testing has mainly been used for measuring chordae mechanical properties (Pokutta-Paskaleva et al., 2019; Prot et al., 2010; Ross et al., 2020), while trabeculae carneae tissue e.g., PMs and myocardium, have been tested in uniaxial (Fatemifar et al., 2018) or biaxial (Fatemifar et al., 2018; Nemavhola, 2017) loading. In this study, we followed the experimental protocols to study the passive mechanical properties of PMs as described in Fatemifar et al. (2018) and for chordae as found in Pokutta-Paskaleva et al. (2019). We are confident that our experimental setup is adequate for the purpose of passive testing, but it should be kept in mind that active properties of PMs are discarded in such settings.

Many early studies distinguished and characterized the structure and mechanical property differences of chordae based on specific chordal types (Lam et al., 1970; Liao and Vesely, 2003; Lomholt et al., 2002). However, recent studies by Zuo et al. (2016) and Pokutta-Paskaleva et al. (2019) showed that chords of differing types vary largely in size

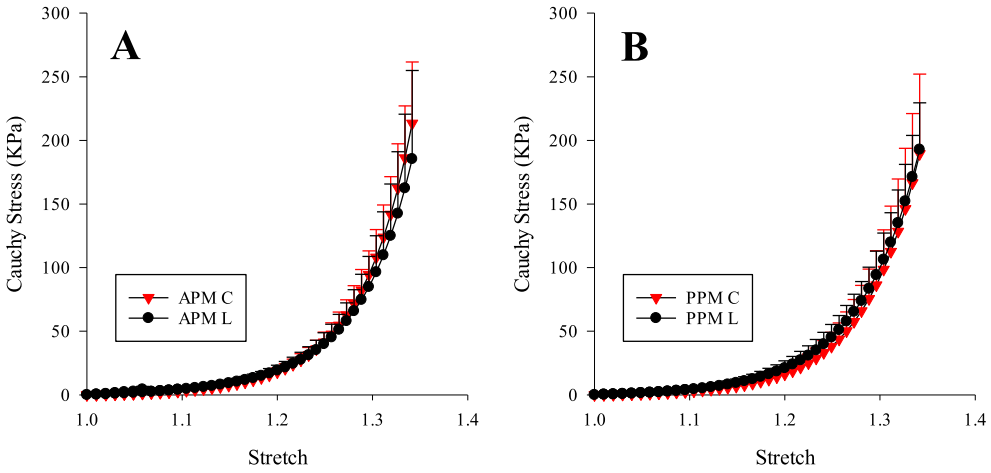

Fig. 12. The mean and standard error of the mean of the Cauchy stress - stretch responses of circumferential (C) and longitudinal (L) direction of APM (A) and PPM (B), respectively.

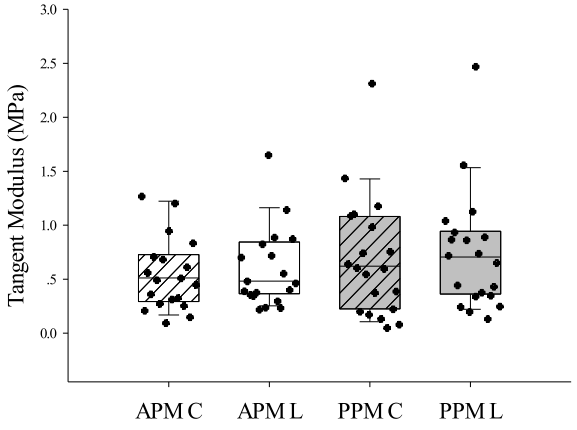

Fig. 13. Average tangent modulus along circumferential and longitudinal direction of both APM and PPM.

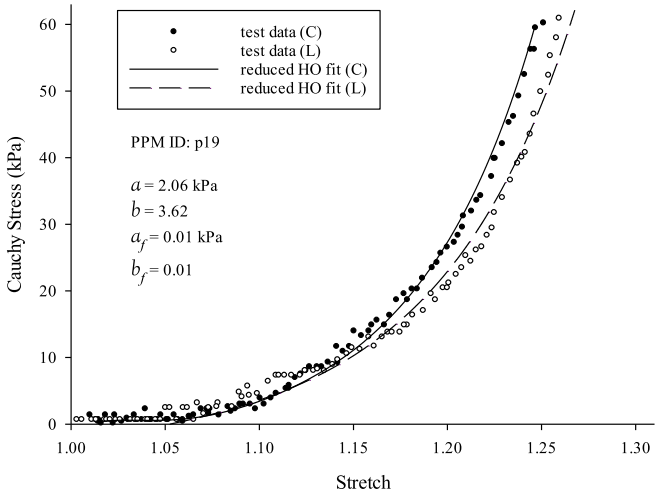

Fig. 14. Cauchy stress - stretch curve of PPM fitted with reduced HO strain energy function under biaxial stretch.

Table 5
The mean and standard deviation of tangent modulus of APM and PPM on circumferential and longitudinal direction.

TM (kPa)	C	L	*p*-value
ALL	631.68 ± 462.48	680.75 ± 470.30	0.32
APM	559.39 ± 336.12	606.84 ± 366.88	0.52
PPM	700.35 ± 557.27	750.96 ± 551.54	0.46
p-value	0.62	0.53	

p-value indicates difference between APM and PPM in row, and difference in circumferential and longitudinal direction in column.

Table 6
The mean and SEM of reduced HO model material parameters for both APM and PPM.

	ALL		APM		PPM	
	Mean	SEM	mean	SEM	mean	SEM
a (kPa)	4.47	0.5	4.38	0.7	4.56	0.9
b	4.46	0.3	4.34	0.4	4.58	0.4
a_f(kPa)	0.67	0.2	0.83	0.4	0.53	0.3
b_f	4.56	1.8	4.61	2.5	4.51	2.8

but do not have significantly different elastic and failure properties. Given that there is an extensive literature available on the mechanical properties of different leaflet types, we focused on the papillary muscle-based classification of chordae, which has not been addressed before. To the best of our knowledge, this study is the first report which documents the biaxial mechanical behaviors of papillary muscle and corresponding chordae tendineae in a porcine model.

The geometry, anatomy, biomechanical properties, histological and micro-structure of PM and connecting chordae tendineae have been studied and quantitatively analyzed. Our results demonstrate that chordae^{PPM} are less in number, but significantly longer and stiffer than chordae^{APM}. The collagen fiber of chordae^{PPM} has larger fibril density but lower fibril diameter than that of chordae^{APM}. The APM and PPM samples were similar in both mechanical and micro-structure properties.

These results indicate that a PM-based classification of chordae should be considered in analysis of MV function or planning surgical treatment. We measured the number, diameter, length, and leaflet coverage ratio of chordae^{APM} and chordae^{PPM} from fresh porcine MV tissue. Our results showed that there are more chords connected to APM than to PPM, and the leaflet coverage ratio of chordae^{APM} is significantly larger than that of chordae^{PPM}. The total number of chords connected to the PM is 17.31 ± 3.28, which is similar to the distribution of human chords (from 15 to 32) (Lam et al., 1970). Overall, the chordae^{PPM} is significantly longer than the chordae^{APM}, which is in accordance with previous observations on strut chordae (Ritchie et al., 2006) and posterior chordae (Lodder

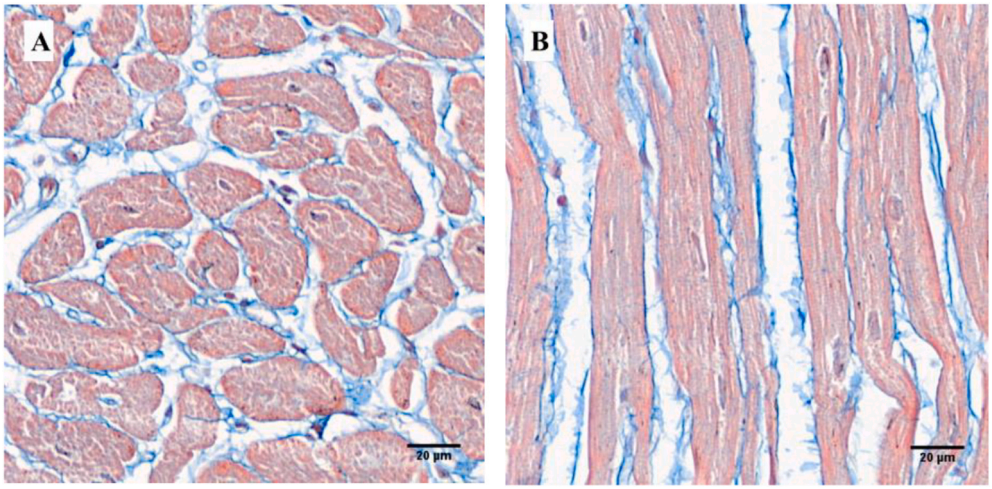

Fig. 15. Masson's trichrome stain of the same PM sample in (A) cross-fiber (circumferential) direction and (B) fiber (longitude) direction. Myocyte diameter and number were measured in perpendicular to longitudinal direction. Myocyte occupation ratio was measured in longitudinal direction.

Table 7
The mean ± standard deviation of myocyte diameter, number, occupation ratio and collagen content of APM and PPM.

	Mean ± +–STD			
	ALL	APM	PPM	*p*-value
Nuclei diameter (um)	18.66 ± 5.48	18.91 ± 5.33	18.41 ± 5.62	0.13
Nuclei number (mm^{-2})	143.94 ± 105.38	149.02 ± 66.50	154.73 ± 133.78	0.86
Occupation ratio (%)	60.08 ± 8.75	59.75 ± 9.31	60.43 ± 8.19	0.64
Collagen content (%)	31.51 ± 6.82	32.99 ± 8.57	29.99 ± 3.94	0.45

p-value indicates difference between APM and PPM.

et al., 2016). The diameter of $chordae^{APM}$ and $chordae^{PPM}$ was similar with a range from 0.36 mm to 1.08 mm. For human chordae, the diameter has been reported varying from 0.36 mm to 1.95 mm (Lim and Boughner, 1975), while for aged human, the range of chord diameter is 0.57 mm–1.27 mm (Zuo et al., 2016). It indicates that the gross anatomy of porcine and human MV chordae is very similar (Lam et al., 1970), which supports the use of porcine MV as a suitable substitute for human tissues for morphological and anatomical analysis.

We tested the chords and PM samples by uniaxial and biaxial tensile tests, respectively. In this study, we have performed a similar DIC system with Zuo et al. (2016), Pokutta-Paskaleva et al. (2019) and Fatemifar et al. (2018) for measuring chordal and PM strain in the uniaxial and biaxial tests. The tangent modulus across all chord samples, ranging from 150 MPa to 600 MPa, is comparable to other studies, reporting values from around 150 MPa–400 MPa for mammals, including ovine (Zuo et al., 2016) and porcine (Pokutta-Paskaleva et al., 2019), and around 300 MPa–400 MPa for aged human (Zuo et al., 2016). When comparing the biomechanical properties of different chord types, the tangent modulus of chordae connected to PPM was significantly higher than that of chordae connected to APM, which means that the stress on $chord^{PPM}$ is higher than that on $chord^{APM}$ under the same stretch; the higher peak tension may associate to high risk of rupture. This observation agrees with the result from the heart simulator study by Nielsen et al. (2003), who reported that the tension on the PPM strut chord was higher than that on the APM strut chord. Lodder et al. (2016) reported that the chordae connected to PPM experienced higher failure force than chordae connected to APM. FEM analysis of a patient-specified MV with chordae model from Wang revealed that in mid systole the APM and PPM force were 4.51N and 5.17N, respectively (Wang and Sun, 2012). The higher stress on chordae connects to PPM may be explained by the mechanical property difference among chordae connected to APM and PPM: while under the same strain the material with higher tangent modulus will experience a higher stress. Although the difference did not reach statistical significance, there is a trend towards less collagen content for PPM than APM. This may also explain why PPM has a higher risk of necrosis and rupture in myocardial ischemia and infarction; this differential risk has been clinically reported and ascribed to differences in coronary artery supply on PMs (Cherian et al., 2014; Yamazaki et al., 2015).

To improve leaflet coaptation and restore the valvular function of diseased valve, it is often necessary to modify the chordal structure (Chikwe and Adams, 2009) by chordal cutting or replacement. For example, treatment of chordal cutting can relieve secondary mitral regurgitation (Messas et al., 2003). Polytetrafluoroethylene (PTFE) sutures (Borgarelli et al., 2017) are commonly used for degenerative mitral valve pathology to replace the native ruptured chordae. Although the artificial suture has high tensile strength and resistance to fatigue, it may change the original cardiac mechanical environment and degenerate, calcify, and eventually rupture as long time outcome (Bortolotti et al., 2012; Ibrahim et al., 2012). In order to optimally design these chordal surgeries, the analysis of native chord biomechanical properties will provide valuable information.

The equal-biaxial test showed no significant differences between APM and PPM, neither did we find any meaningful differences in the properties along the circumferential or longitudinal direction which was also observed by Fatemifar et al. (2018) on biomechanical properties of human patient PM samples in a physiological loading range. They revealed the equi-biaxial tangent modulus ratio of human left ventricle papillary muscles was approximate to 1.3, similar to the mean ratio of 1.07 (680.75 kPa/631.68 kPa) of our study.

In our study, chordae and PM tissue are regarded as hyper-elastic, anisotropic, and incompressible material. This has been evaluated and established in experiments by Demer and Yin (1983), who have tested myocardium tissue to various levels of hydrostatic stress and calculated associated volumetric strains to reach this conclusion. Such an assumption is also commonly applied in many experimental studies e.g., Holzapfel and Ogden (2009); Sommer et al. (2015); and Fatemifar et al. (2018). In our chordal experiments, only one camera was used to track the fiducial markers, which would allow us to measure the separation of fiducial markers and the width of chordal cross-section, but lack of measurements in the depth direction. Therefore, it is difficult to quantify the "deformed cross-sectional area" in the current experimental setting.

Considering many existing studies have assumed incompressibility for various mitral valve apparatus, chordae (Pokutta-Paskaleva et al., 2019; Ross et al., 2020; Zuo et al., 2016) and PM (Fatemifar et al., 2018) included, we applied the same assumption in this study. In order to calculate the stresses in the marker region, we assumed that the specimen had a uniform diameter and the force applied at the edge was uniformly distributed. Local non-homogeneous areas of the sample may induce under-estimation or over-estimation of the stress. In our study, we carefully chose samples with uniform diameter, and our measurements at random locations showed only a 5.5% difference in diameter along the sample length.

Histological assessments of Masson's trichrome staining revealed that the collagen core area occupation ratio of chordae^{PPM} is significantly larger than that of chordae^{APM}. The more collagen the chordae contain, the stiffer the chordae would be (Sedransk et al., 2002). This is in accordance with our experimental results, demonstrating that chordae^{PPM} is significantly stiffer than the chordae^{APM}. From TEM images, we calculated the collagen fibril average diameter, fibril density and fibril area ratio of the chord samples. The average collagen fibril diameter of chordae^{APM} is significantly larger than that of chordae^{PPM} ($p < 0.001$), but the collagen fibril density of chordae^{APM} is significantly smaller than that of chordae^{PPM} ($p < 0.001$). As such, the fibril area ratio was not different between the two chordae families. Both the collagen fibril average diameter and density are in a similar range as previously reported by Liao and Vesely (2003).

The higher fibril density may provide more strength when under large load, which corresponds to higher stiffness in chordae on PPM side. From Liao and Vesely (2003), the inter-fibrillar proteoglycans (PGs) plays an important role in shear force transfer, so a higher density of fibrils have dense amount of PGs, which may lead to higher stiffness. Our results have shown the same trend as Liao's conclusion. The microstructure of PM nuclei including the myocyte cell diameter, quantity of cells with nucleus and the occupation ratio of cells is not significantly different between APM and PPM. The amount of collagen is related to the passive mechanical properties of tissue (Voorhees and Han, 2014), and similar collagen content on both PMs would explain the similarity in mechanical behavior of PM samples.

In this study, we further fitted our experimental data to different strain energy functions. The hyper-elastic strain energy functions can adequately describe the nonlinear, anisotropic stress–strain behavior of the chords and the PMs properly. The selected strain energy functions for chordae and PMs are mostly widely used ones in the modeling communities (Gao et al., 2015; Guan et al., 2019; Sack et al., 2018). Further improvement in strain energy functions could be done by incorporating more detailed microstructures, such as the content and wrinkles of collagen network, which is beyond the scope of this study. We also notice that for some PM samples, the standard deviation of estimated parameters from 50 random generated initial values are not small (Appendix Table A2), but this is not the case for the chordae samples because of the relatively simple formulation of the Ogden model compared to the reduced HO model. This suggests that for some PM samples, it can be challenging to infer the four parameters of the reduced HO model uniquely. Potential reasons include (1) the intrinsic correlation among the parameters; (2) insufficient experimental data to capture the nonlinear responses, for example, stretching further or including other experiments (uniaxial or shearing, etc) could be helpful in determining the material parameters of PM samples. Future studies are needed to determine the optimal experimental combinations for characterizing PM mechanical properties.

Patient-specific computational models of the mitral valve with chordae have been developed and studied to understand the dynamics of valve function recently. For example, Wang and Sun (2012) reconstructed and simulated the MV with chordae from CT images. Gao et al. (2014) developed a framework of patient-specific fluid-structure interaction MV model with simplified chordae using immersed boundary method. (2017); Toma et al. (2016) simulated the MV with detailed chordal structure to analyze the distinct role played by individual chordae in closure of the mitral valve leaflets. However, none of these studies considered the PMs and the differences between chordae^{APM} and chordae^{PPM}. Our study will help improve the accuracy of modelling of the MV.

5. Limitations

No human samples were used for this study, which is difficult considering the rarity of the material. It cannot be excluded that porcine tissue differs from human tissue, but it has been widely used as a substitution material for better understanding human tissue behavior. The experimental set-up did not allow to assess active properties of papillary muscle, and the contribution of active properties of papillary muscle had not been considered in this work. A further limitation is the qualitative nature of the histology assessment through image analysis. Soft tissue may shrink after dehydration in preparation of histology sample, thus we adopted the collagen and elastin ratio to avoid this artefact. A more rigorous collagen and PGs content analysis will be considered as a future effort to more accurately characterize the mechanical behavior differences in chordae^{APM} and chordae^{PPM} samples.

CRediT authorship contribution statement

Shengda Chen: Visualization, Writing - original draft, Software, Investigation, Formal analysis. **Candra Ratna Sari:** Data curation, Investigation. **Hao Gao:** Visualization, Software. **Yang Lei:** Data curation. **Patrick Segers:** Writing - review & editing. **Matthieu De Beule:** Writing - review & editing. **Guixue Wang:** Supervision. **Xingshuang Ma:** Software, Investigation, Validation, Methodology, Writing - review & editing, Supervision.

Declaration of competing interest

Matthieu De Beule is shareholder of FEops.

Acknowledgement

The authors acknowledge the financial support from the National Natural Science Foundation of China [No.11532004, 11402041, 11871399], the Fundamental Research Funds for the Central Universities [2018CDXYSW0023] and funding from the UK EPSRC (EP/N014642/1). The biaxial tensile test was operated on National Engineering Research Center for Biomaterials in Sichuan University. Authors would like to deliver special thanks to their director, Prof. Yunbing Wang for his support. We would also like to thank Debao Guan for data analysis supports.

Appendix A

Table A1
Estimated Ogden model parameters for all chordal samples. 'a' stands for chordae on anterior papillary muscle side, 'p' stands for chordae on posterior papillary muscle side.

	μ (kPa)		A	
Sample ID	mean	STD	mean	STD
a1	0.080085	4.54E-02	112.9152	4.91E+01
a2	2.581778	5.68E-05	29.13658	6.59E-04
a3	8.862465	1.45E-04	12.89839	2.75E-04
a4	34.05483	3.91E-05	2.061975	4.44E-06
a5	2.041693	8.61E-05	84.34013	2.96E-03
a6	11.24527	4.63E-05	42.42803	2.55E-04
a7	0.056691	9.77E-08	24.95574	2.22E-05
a8	2.226956	7.08E-05	95.32322	2.75E-03
a9	4.402054	6.38E-06	21.14173	3.65E-05
a10	0.147095	8.09E-03	64.98718	2.24E+00
a11	17.39551	1.84E-05	14.17615	2.43E-05
a12	0.067039	4.07E-06	61.51572	2.92E-03
a13	35.5606	1.40E-04	1.560601	1.64E-05
a14	7.027133	4.34E-05	41.98636	3.37E-04
a15	31.94181	1.76E-04	2.931248	3.87E-05
a16	10.1916	7.86E-05	26.96147	2.88E-04
a17	14.47643	6.83E-05	14.10108	1.01E-04
a18	0.291922	1.39E-02	90.26954	1.69E+00
a19	0.080694	1.47E-06	51.46801	6.11E-04
a20	7.922476	4.07E-05	11.64143	9.50E-05
a21	0.128549	1.38E-02	64.37465	4.99E+00
a22	0.338121	8.61E-02	75.97644	2.72E+00
a23	15.91973	1.77E-05	9.297103	1.78E-05
a24	0.15704	1.11E-05	81.25646	3.91E-03
p1	1.151121	1.50E-06	44.31482	4.19E-05
p2	2.366764	2.15E-05	55.44715	4.85E-04
p3	9.601672	5.19E-05	21.41908	1.48E-04
p4	5.819605	3.89E-05	30.44917	2.17E-04
p5	0.906229	1.47E-04	200.8943	9.12E-03
p6	0.255065	1.30E-06	128.6804	4.18E-04
p7	12.51755	1.62E-03	18.07526	3.43E-03
p8	34.01276	5.24E-04	5.827741	1.68E-04
p9	17.47935	1.05E-04	24.9022	2.03E-04
p10	22.69692	1.00E-03	7.897498	6.32E-04
p11	17.84665	2.69E-04	23.73615	5.62E-04
p12	20.23919	1.58E-04	14.19758	1.80E-04
p13	0.342335	2.37E-05	143.9491	4.47E-03
p14	3.49016	7.86E-05	69.09096	1.62E-03
p15	13.38007	3.83E-05	18.08737	8.20E-05
p16	14.90215	5.86E-06	14.41115	9.14E-06
p17	13.34149	5.09E-05	7.433231	5.37E-05
p18	3.339417	1.76E-04	49.83198	2.92E-03
p19	24.38073	3.36E-04	8.296726	1.93E-04
p20	3.117933	1.38E-02	142.6113	6.31E-01

Table A2
Estimated Reduced HO model parameters for all papillary muscle samples. 'a' stands for anterior papillary muscle side, 'p' stands for posterior papillary muscle side.

	a (kPa)		b		a_f(kPa)		b_f	
Sample ID	mean	STD	mean	STD	mean	STD	mean	STD
a1	1.96	7.40E-05	5.90	8.52E-05	2.82	1.94E-04	9.24	3.55E-04
a2	2.45	7.17E+00	3.38	2.24E+00	2.43	6.01E+00	3.90	8.27E+00
a3	4.21	6.73E-04	3.78	3.30E-04	0.42	1.42E-03	5.54	1.31E-02
a4	4.05	2.37E-05	4.68	1.23E-05	0.01	5.83E-08	0.01	5.19E-07
a5	7.30	1.26E-05	3.49	5.14E-07	0.01	6.92E-08	0.01	4.46E-06
a6	1.98	3.39E+00	4.89	4.61E+00	1.19	7.00E-01	4.12	2.87E+00
a7	5.92	5.07E-05	3.13	1.99E-05	0.01	5.61E-08	0.01	1.81E-06
a8	2.79	1.29E-01	3.72	6.92E-02	0.01	1.27E-02	0.02	4.83E-02
a9	2.87	3.42E-05	4.10	3.84E-05	0.01	7.33E-08	0.01	1.71E-06
a10	5.33	1.42E-05	5.44	1.19E-06	0.01	8.06E-08	0.01	8.22E-07
a11	3.58	7.49E-05	4.37	3.53E-05	0.01	7.65E-08	0.01	9.44E-07
a12	2.34	1.74E-01	3.93	1.45E-01	7.30	1.33E-01	3.81	8.72E-02
a13	9.86	4.70E-05	7.19	1.99E-05	0.01	1.58E-07	0.01	3.15E-06
a14	11.97	7.01E-04	2.39	1.14E-04	0.49	2.39E-03	45.51	6.85E-02
a15	5.53	4.84E-05	3.57	1.57E-05	0.01	8.99E-08	0.01	1.30E-06
a16	2.82	3.51E-01	3.71	2.91E-01	0.06	3.00E-01	0.01	3.38E-06
a17	1.77	8.57E-01	3.21	1.21E+00	0.90	3.58E-01	0.01	8.17E-07
a18	0.97	5.85E-05	9.19	1.63E-04	0.01	5.35E-08	0.01	1.75E-07
a19	5.51	2.76E-01	2.46	9.01E-02	0.07	2.73E-01	15.32	3.55E+00
p1	2.52	1.6E-01	4.78	1.1E-01	4.71	1.0E+00	5.16	1.1E+00

(*continued on next page*)

Table A2 (*continued*)

	a (kPa)		b		a_f(kPa)		b_f	
p2	2.48	3.2E-04	7.77	3.3E-04	0.38	1.5E-03	53.69	8.8E-02
p3	1.43	2.3E-03	4.48	2.0E-03	0.01	3.5E-08	0.01	5.0E-07
p4	2.78	4.2E-06	6.58	3.6E-06	0.01	2.9E-08	0.01	1.9E-05
p5	18.56	1.5E-04	3.34	2.0E-05	0.01	1.0E-07	0.01	1.2E-05
p6	8.16	3.1E-04	2.44	6.9E-05	2.10	6.8E-04	3.98	1.0E-03
p7	2.73	6.8E-05	7.56	1.2E-04	0.01	5.1E-08	0.01	1.7E-05
p8	4.51	1.5E+00	4.31	4.1E-01	0.07	2.9E-01	0.22	9.1E-01
p9	6.02	1.6E-05	7.98	8.4E-06	0.01	8.4E-08	0.01	6.5E-07
p10	3.70	2.5E-05	3.46	1.5E-05	0.01	1.9E-08	0.01	1.1E-06
p11	5.94	2.7E-01	5.67	1.4E-01	0.01	3.9E-08	0.01	9.2E-07
p12	4.50	1.1E-04	5.54	7.9E-05	0.01	5.6E-08	0.01	4.7E-07
p13	9.04	6.2E-04	5.08	1.8E-04	0.35	9.4E-04	19.05	1.9E-02
p14	5.73	7.4E-05	2.93	2.6E-05	0.01	9.6E-08	0.01	2.7E-06
p15	2.26	1.2E+00	3.63	1.2E+00	0.18	5.8E-01	0.59	2.2E+00
p16	2.98	7.4E-05	1.99	4.5E-05	0.01	2.0E-08	0.01	5.9E-08
p17	1.44	3.6E-01	3.46	4.2E-01	2.40	1.1E+00	6.95	1.5E+00
p18	1.87	3.8E-05	4.45	4.3E-05	0.01	2.5E-08	0.01	8.3E-07
p19	2.06	7.4E-01	3.62	1.4E+00	0.01	3.5E-04	0.01	3.2E-07
p20	2.52	1.2E+00	2.48	1.7E+00	0.19	4.9E-01	0.41	1.3E+00

References

Adams, J., O'Rourke, M.J., 2015. In vitro measurement of the coaptation force distribution in normal and functional regurgitant porcine mitral valves. J. Biomech. Eng. 137.

Askov, J.B., Honge, J.L., Jensen, M.O., Nygaard, H., Hasenkam, J.M., Nielsen, S.L., 2013. Significance of force transfer in mitral valve-left ventricular interaction: in vivo assessment. J. Thorac. Cardiovasc. Surg. 145, 1635–1641, 1641.e1631-1641, 1641.e1631.

Askov, J.B., Honge, J.L., Nygaard, H., Hasenkam, J.M., Nielsen, S.L., Jensen, M.O., 2011. Papillary muscle force transducer for measurement in vivo. Cardiovasc. Eng. Technol. 2, 196–202.

Borgarelli, M., Lanz, O., Pavlisko, N., Abbott, J.A., Menciotti, G., Aherne, M., Lahmers, S. M., Lahmers, K.K., Gammie, J.S., 2017. Mitral valve repair in dogs using an ePTFE chordal implantation device: a pilot study. J. Vet. Cardiol. 19, 256–267.

Bortolotti, U., Milano, A.D., Frater, R.W.M., 2012. Mitral valve repair with artificial chordae: a review of its history, technical details, long-term results, and pathology. Ann. Thorac. Surg. 93, 684–691.

Chen, W., Gao, C., Zhang, D., Wang, L., Qiu, Z., 2018. A new biaxial tensile shear test method to measure shear behaviour of coated fabrics for architectural use. Compos. Struct. 203, 943–951.

Cherian, P.S., Clarke, A.J.B., Burstow, D.J., 2014. Unusual case of acute posteromedial papillary muscle rupture after acute anterior myocardial infarction. Heart Lung Circ. 23, e16–e19.

Chikwe, J., Adams, D.H., 2009. State of the art: degenerative mitral valve disease. Heart Lung Circ. 18, 319–329.

Demer, L.L., Yin, F.C., 1983. Passive biaxial mechanical properties of isolated canine myocardium. J. Physiol. (Camb.) 339, 615–630.

Fan, R., Sacks, M.S., 2014. Simulation of planar soft tissues using a structural constitutive model: finite element implementation and validation. J. Biomech. 47, 2043–2054.

Fatemifar, F., Feldman, M., Oglesby, M., Han, H.C., 2018. Comparison of biomechanical properties and microstructure of trabeculae carneae, papillary muscles, and myocardium in human heart. J. Biomech. Eng. 141 (2) https://doi.org/10.1115/1.4041966.

Gabbay, U., Yosefy, C., 2010. The underlying causes of chordae tendinae rupture: a systematic review. Int. J. Cardiol. 143, 113–118.

Gammie, J.S., Bartus, K., Gackowski, A., D'Ambra, M.N., Szymanski, P., Bilewska, A., Kusmierczyk, M., Kapelak, B., Rzucidlo-Resil, J., Moat, N., Duncan, A., Yadev, R., Livesey, S., Diprose, P., Gerosa, G., D'Onofrio, A., Pitterello, D., Denti, P., La Canna, G., De Bonis, M., Alfieri, O., Hung, J., Kolsut, P., 2018. Beating-heart mitral valve repair using a novel ePTFE cordal implantation device: a prospective trial. J. Am. Coll. Cardiol. 71, 25–36.

Gao, H., Li, W.G., Cai, L., Berry, C., Luo, X.Y., 2015. Parameter estimation in a Holzapfel-Ogden law for healthy myocardium. J. Eng. Math. 95, 231–248.

Gao, H., Ma, X., Qi, N., Berry, C., Griffith, B.E., Luo, X., 2014. A finite strain nonlinear human mitral valve model with fluid-structure interaction. Int. J. Numer. Method. Biomed. Eng. 30, 1597–1613.

Guan, D., Ahmad, F., Theobald, P., Soe, S., Luo, X., Gao, H., 2019. On the AIC-based model reduction for the general Holzapfel–Ogden myocardial constitutive law. Biomech. Model. Mechanobiol. 18, 1213–1232.

Holzapfel, A.G., 2000. Nonlinear Solid Mechanics II. John Wiley \& Sons, Inc.

Holzapfel, G.A., Ogden, R.W., 2009. Constitutive modelling of passive myocardium: a structurally based framework for material characterization. Philos. Transact. A Math. Phys. Eng. Sci. 367, 3445–3475.

Holzapfel, G.A., Ogden, R.W., 2010. Modelling the layer-specific three-dimensional residual stresses in arteries, with an application to the human aorta. J. R. Soc. Interface 7, 787–799.

Ibrahim, M., Rao, C., Athanasiou, T., 2012. Artificial chordae for degenerative mitral valve disease: critical analysis of current techniques. Interact. Cardiovasc. Thorac. Surg. 15, 1019–1032.

Jett, S., Laurence, D., Kunkel, R., Babu, A.R., Kramer, K., Baumwart, R., Towner, R., Wu, Y., Lee, C.-H., 2018. An investigation of the anisotropic mechanical properties and anatomical structure of porcine atrioventricular heart valves. Journal of the mechanical behavior of biomedical materials 87, 155–171.

Kunzelman, K.S., Cochran, R.P., 1990. Mechanical properties of basal and marginal mitral valve chordae tendineae. ASAIO (Am. Soc. Artif. Intern. Organs) Trans. 36, M405–M408.

Kunzelman, K.S., Cochran, R.P., Verrier, E.D., Eberhart, R.C., 1994. Anatomic basis for mitral valve modelling. J. Heart Valve Dis. 3, 491–496.

Lam, J.H.C., Ranganathan, N., Wigle, E.D., Silver, M.D., 1970. Morphology of the human mitral valve. Circulation 41, 459–467.

Laurence, D., Ross, C., Jett, S., Johns, C., Echols, A., Baumwart, R., Towner, R., Liao, J., Bajona, P., Wu, Y., Lee, C.H., 2019. An investigation of regional variations in the biaxial mechanical properties and stress relaxation behaviors of porcine atrioventricular heart valve leaflets. J. Biomech. 83, 16–27.

Liao, J., Vesely, I., 2003. A structural basis for the size-related mechanical properties of mitral valve chordae tendineae. J. Biomech. 36, 1125–1133.

Liao, J., Vesely, I., 2007. Skewness angle of interfibrillar proteoglycans increases with applied load on mitral valve chordae tendineae. J. Biomech. 40, 390–398.

Lim, K.O., Boughner, D.R., 1975. Mechanical properties of human mitral valve chordae tendineae: variation with size and strain rate. Can. J. Physiol. Pharmacol. 53, 330–339.

Lodder, J., Verkerke, G.J., Delemarre, B.J.M., Dodou, D., 2016. Morphological and mechanical properties of the posterior leaflet chordae tendineae in the mitral valve. Proc. Inst. Mech. Eng. H 230, 77–84.

Lomholt, M., Nielsen, S.L., Hansen, S.B., Andersen, N.T., Hasenkam, J.M., 2002. Differential tension between secondary and primary mitral chordae in an acute in-vivo porcine model. J. Heart Valve Dis. 11, 337–345.

Messas, E., Pouzet, B., Touchot, B., Guerrero, J.L., Vlahakes, G.J., Desnos, M., Menasche, P., Hagege, A., Levine, R.A., 2003. Efficacy of chordal cutting to relieve chronic persistent ischemic mitral regurgitation. Circulation 108 (Suppl. 1), II111–115.

Millard, L., Espino, D.M., Shepherd, D.E.T., Hukins, D.W.L., Buchan, K.G., 2011. Mechanical properties of chordae tendineae of the mitral valve: young's modulus, structural stiffness, and effects of aging. J. Mech. Med. Biol. 11, 221–230.

Morris, L., Desai, A., Akkus, N.I., 2015. Anterolateral papillary muscle rupture after intervention of the right coronary artery. Rev. Port. Cardiol. 34, 693.e691-693.e693.

Nemavhola, F., 2017. Biaxial quantification of passive porcine myocardium elastic properties by region. Eng. Solid Mec. 5, 155–166.

Nielsen, S.L., Hansen, S.B., Nielsen, K.O., Nygaard, H., Paulsen, P.K., Hasenkam, J.M., 2005. Imbalanced chordal force distribution causes acute ischemic mitral regurgitation: mechanistic insights from chordae tendineae force measurements in pigs. J. Thorac. Cardiovasc. Surg. 129, 525–531.

Nielsen, S.L., Lomholt, M., Johansen, P., Hansen, S.B., Andersen, N.T., Hasenkam, J.M., 2011. Mitral ring annuloplasty relieves tension of the secondary but not primary chordae tendineae in the anterior mitral leaflet. J. Thorac. Cardiovasc. Surg. 141, 732–737.

Nielsen, S.L., Timek, T.A., Green, G.R., Dagum, P., Daughters, G.T., Hasenkam, J.M., Bolger, A.F., Ingels, N.B., Miller, D.C., 2003. Influence of anterior mitral leaflet second-order chordae tendineae on left ventricular systolic function. Circulation 108, 486–491.

Ogden, R.W., 1997. Non-linear Elastic Deformations. Dover Publications.

Pham, T., Sulejmani, F., Shin, E., Wang, D., Sun, W., 2017. Quantification and comparison of the mechanical properties of four human cardiac valves. Acta Biomater. 54, 345–355.

Pokutta-Paskaleva, A., Sulejmani, F., DelRocini, M., Sun, W., 2019. Comparative mechanical, morphological, and microstructural characterization of porcine mitral and tricuspid leaflets and chordae tendineae. Acta Biomater. 85, 241–252.

Prot, V., Skallerud, B., Sommer, G., Holzapfel, G.A., 2010. On modelling and analysis of healthy and pathological human mitral valves: two case studies. J. Mech. Behav. Biomed. Mater. 3, 167–177.

Ritchie, J., Jimenez, J., He, Z., Sacks, M.S., Yoganathan, A.P., 2006. The material properties of the native porcine mitral valve chordae tendineae: an in vitro investigation. J. Biomech. 39, 1129–1135.

Ritchie, J., Warnock, J.N., Yoganathan, A.P., 2005. Structural characterization of the chordae tendineae in native porcine mitral valves. Ann. Thorac. Surg. 80, 189–197.

Ross, C.J., Laurence, D.W., Hsu, M.-C., Baumwart, R., Zhao, Y.D., Mir, A., Burkhart, H. M., Holzapfel, G.A., Wu, Y., Lee, C.-H., 2020. Mechanics of porcine heart valves' strut chordae tendineae investigated as a leaflet–chordae–papillary muscle entity. Ann. Biomed. Eng. 48 (5), 1463–1474. https://doi.org/10.1007/s10439-020-02464-6.

Sack, K.L., Aliotta, E., Ennis, D.B., Choy, J.S., Kassab, G.S., Guccione, J.M., Franz, T., 2018. Construction and validation of subject-specific biventricular finite-element models of healthy and failing swine hearts from high-resolution DT-MRI. Front. Physiol. 9, 539-539.

Sedransk, K.L., Grande-Allen, K.J., Vesely, I., 2002. Failure mechanics of mitral valve chordae tendineae. J. Heart Valve Dis. 11, 644–650.

Sommer, G., Schriefl, A.J., Andrä, M., Sacherer, M., Viertler, C., Wolinski, H., Holzapfel, G.A., 2015. Biomechanical properties and microstructure of human ventricular myocardium. Acta Biomater. 24, 172–192.

Stefanovski, D., Walfisch, A., Kedev, S., Tager, S., 2012. Isolated right coronary lesion and anterolateral papillary muscle rupture - case report and review of the literature. J. Cardiothorac. Surg. 7.

Toma, M., Bloodworth, C.H., Pierce, E.L., Einstein, D.R., Cochran, R.P., Yoganathan, A. P., Kunzelman, K.S., 2017. Fluid-structure interaction analysis of ruptured mitral chordae tendineae. Ann. Biomed. Eng. 45, 619–631.

Toma, M., Einstein, D.R., Bloodworth, C.H., Cochran, R.P., Yoganathan, A.P., Kunzelman, K.S., 2016. Fluid-structure interaction and structural analyses using a comprehensive mitral valve model with 3D chordal structure. Int. J. Numer. Method. Biomed. Eng. 33 e2815-e2815.

Tong, J., Cohnert, T., Regitnig, P., Holzapfel, G.A., 2011. Effects of age on the elastic properties of the intraluminal thrombus and the thrombus-covered wall in abdominal aortic aneurysms: biaxial extension behaviour and material modelling. Eur. J. Vasc. Endovasc. Surg. 42, 207–219.

Urheim, S., Edvardsen, T., Torp, H., Angelsen, B., Smiseth, O.A., 2000. Myocardial strain by Doppler echocardiography. Validation of a new method to quantify regional myocardial function. Circulation 102, 1158–1164.

Voorhees, A.P., Han, H.C., 2014. A model to determine the effect of collagen fiber alignment on heart function post myocardial infarction. Theor. Biol. Med. Model. 11, 6.

Wang, Q., Sun, W., 2012. Finite element modeling of mitral valve dynamic deformation using patient-specific multi-slices computed tomography scans. Ann. Biomed. Eng. 41, 142–153.

Yamazaki, M., Fukui, T., Mahara, K., Takanashi, S., 2015. Complete rupture of the anterolateral papillary muscle caused by coronary spasm. Interact. Cardiovasc. Thorac. Surg. 20 (6), 798–800. https://doi.org/10.1093/icvts/ivv237 ivv237-ivv237.

Zuo, K., Pham, T., Li, K., Martin, C., He, Z., Sun, W., 2016. Characterization of biomechanical properties of aged human and ovine mitral valve chordae tendineae. J. Mech. Behav. Biomed. Mater. 62, 607–618.